A&A 657, A41 (2022)
https://doi.org/10.1051/0004-6361/202141347

Astronomy & Astrophysics

The outermost stellar halo of NGC 5128 (Centaurus A): Radial structure*

M. Rejkuba[1], W. E. Harris[2], L. Greggio[3], D. Crnojević[4], and G. L. H. Harris[5]

[1] European Southern Observatory, Karl-Schwarzschild Strasse 2, 85748 Garching, Germany
e-mail: mrejkuba@eso.org
[2] Department of Physics and Astronomy, McMaster University, Hamilton, ON L8S 4M1, Canada
[3] INAF, Osservatorio Astronomico di Padova, Vicolo dell'Osservatorio 5, 35122 Padova, Italy
[4] University of Tampa, Department of Chemistry, Biochemistry, and Physics, 401 West Kennedy Boulevard, Tampa, FL 33606, USA
[5] Department of Physics and Astronomy, University of Waterloo, Waterloo, ON N2L 3G1, Canada

Received 19 May 2021 / Accepted 24 September 2021

ABSTRACT

Context. The extended stellar halos of galaxies contain important clues for investigating their assembly history and evolution.
Aims. We investigate the resolved stellar content and the extended halo of NGC 5128 as a function of galactocentric distance, and trace the halo outward to its currently detectable limits.
Methods. We used *Hubble* Space Telescope images obtained with the WFPC2, ACS, and WFC3 cameras equipped with $F606W$ and $F814W$ filters to resolve individual red giant branch (RGB) stars in 28 independent pointings across the halo of NGC 5128. The stellar halo analysis for 14 of these pointings is presented here for the first time. Star counts from deep VI color-magnitude diagrams reaching at least 1.5 mag below the tip of the RGB are used to derive the surface density distribution of the halo. The contamination by Milky Way stars is assessed with a new control field, with models, and by combining optical and near-IR photometry.
Results. We present a new calibration of the WFC3 $F606W$ + $F814W$ photometry to the ground-based VI photometric system. The photometry shows that the stellar halo of NGC 5128 is dominated by old RGB stars that are present in all fields. The V-band surface brightness of fields changes from 23 to 32 mag arcsec^{-2} between the innermost field only 8.3 kpc from the galaxy center to our outermost halo fields, which are located 140 kpc away from the center along the major axis and 92 kpc along the minor axis. Within the inner ∼30 kpc, we also find evidence for a 2−3 Gyr old population traced by asymptotic giant branch stars that are brighter than the tip of the RGB. This population contributes only up to 10% in total stellar mass if it is 2 Gyr old, but a larger fraction of 30–40% is required if its age is 3 Gyr. The stellar surface density profile is well fit by a classic $r^{1/4}$ curve or a simple power-law form $\sim r^{-3.1}$ over the full radial range, with no obvious break in the slope, but with large field-to-field scatter. The ellipticity measured from integrated-light photometry in the inner parts, $e = (b/a) = 0.77$, flattens to $e = 0.54 \pm 0.02$ beyond 30 kpc. Considering the flattening of the outer halo, the projection of the elliptical isophote on the semimajor axis for our most distant field reaches nearly 30 effective radii.

Key words. galaxies: elliptical and lenticular, cD – galaxies: individual: NGC 5128 – galaxies: stellar content

1. Introduction

We have long known that the halo of our own Milky Way galaxy extends over many kiloparsecs and that it is principally populated with metal-poor stars (Eggen et al. 1962; Searle & Zinn 1978; Freeman 1987). The high level of inhomogeneity, the clear presence of stellar streams and substructure, and the possible dual nature of the halos of Milky Way and M 31 are among the more recent results that have changed our understanding of galaxy halo assembly (e.g., Ferguson et al. 2002; Belokurov et al. 2006; Carollo et al. 2007; Bell et al. 2008; Sesar et al. 2011; Drake et al. 2013; Ibata et al. 2014).

A major difference for studies of stellar halos around nearby galaxies beyond the Local Group was made by the high resolution and high sensitivity of the *Hubble* Space Telescope (HST) cameras, which can resolve and measure individual halo stars routinely in galaxies at distances out to about 10 Mpc (Harris et al. 2007a; Rejkuba et al. 2011; Peacock et al. 2015; Monachesi et al. 2016; Cohen et al. 2020). With special efforts to accumulate longer exposure times, galaxies out to the distance of the Virgo system are within reach (Williams et al. 2007; Bird et al. 2010). Direct starcounts of RGB stars make a highly effective route to tracing the halo population outward to levels of equivalent surface brightness that are difficult to achieve by other means (e.g., Pritchet & van den Bergh 1994; Harris et al. 2007b; Gilbert et al. 2012; Harmsen et al. 2017, in addition to the papers cited above). Integrated-light studies can be quite effective at identifying the spatial distribution and structure of the halo (Mihos et al. 2013; Duc et al. 2015; Merritt et al. 2016; Iodice et al. 2016, 2019; Bílek et al. 2020), in spite of challenging photometry at extremely low surface brightness levels (see Mihos 2019 for a recent review of advances and challenges related to deep imaging of diffuse light around galaxies). However, integrated-light studies do not allow an unambiguous description of the properties of the stellar populations because of the age-metallicity degeneracy (see, e.g., Mihos et al. 2013), and furthermore, they do not give information on the distributions

* Photometry data tables are only available at the CDS via anonymous ftp to cdsarc.u-strasbg.fr (130.79.128.5) or via http://cdsarc.u-strasbg.fr/viz-bin/cat/J/A+A/657/A41

of age and metallicity. These underlying distributions can be addressed by analyzing the color-magnitude diagram (CMD) of resolved stars.

Even with the HST, only a few large early-type galaxies (ETGs) are especially amenable to resolved stellar population studies. Of these, NGC 5128 (often referred to by its well-known radio source designation Centaurus A or Cen A) has a special place: At a distance of 3.8 Mpc (Rejkuba 2004; Harris et al. 2010), it is by far the nearest easily observable giant ETG. Because of its proximity, NGC 5128 was the first giant ETG to have its stellar halo resolved into individual red giant branch (RGB) stars (Soria et al. 1996), and it has since been observed with the HST within several programs. It has also been imaged under very good seeing conditions from the ground.

Several earlier studies concentrated on the visible star formation in the inner halo (Fassett & Graham 2000; Mould et al. 2000; Rejkuba et al. 2001, 2002; Graham & Fassett 2002; Peng et al. 2002; Crockett et al. 2012), which is associated with the so-called inner and outer filaments (Blanco et al. 1975; Santoro et al. 2015) and is possibly triggered by the radio jet (Oosterloo & Morganti 2005). Although visibly quite prominent, these features contain only a small fraction of the halo mass (Rejkuba et al. 2004; Oosterloo & Morganti 2005), have a low star formation efficiency (Salomé et al. 2016), and are confined to a region extending out to ≃35 kpc along the northeastern major axis (Neff et al. 2014). Within a radius of ∼20 kpc lie also well-known shells around the galaxy (Malin et al. 1983; Peng et al. 2002) that were likely formed during a past accretion of a companion galaxy that deposited the gas and dust that has long been noted as a characteristic of NGC 5128 (Charmandaris et al. 2000). Struve et al. (2010) pointed out that the HI fraction in Centaurus A ($M_{\rm HI}/L_B = 0.01$) is rather low for an ETG, suggesting that the most recent accretion involved a relatively small (Small Magellanic Cloud like) galaxy about $1.6-3.2 \times 10^8$ yr ago. An alternative major-merger origin was proposed by numerical simulations that reproduced some selected properties of NGC 5128 (Bekki & Peng 2006; Wang et al. 2020). Setting this in a broader context: Tal et al. (2009) found that 73% of nearby luminous elliptical galaxies show tidal disturbance signatures in their stellar bodies; similar results are evident from the MATLAS survey (Duc et al. 2015). Thus NGC 5128, far from being "peculiar", is a quite typical giant elliptical (see also the review of Harris 2010).

A systematic survey of the stellar halo properties in NGC 5128 was performed with HST imaging that reached at least 1.5 mag below the RGB tip (TRGB), deep enough to sample its full metallicity distribution. This survey started with the works of G. Harris and Collaborators over 20 years ago. Inner- and mid-halo fields were observed with the WFPC2 camera at 8, 21, and 31 kpc distance from the center (Harris et al. 1999; Harris & Harris 2000, 2002), establishing for the first time a (then) surprisingly broad metallicity distribution of the halo RGB stars, with a peak metallicity close to solar in the innermost field and only mildly subsolar in the other two fields. Low-metallicity stars reaching [Fe/H] ≃ −2 dex are present in all these fields, but are very much in the minority.

After the HST servicing mission 3B and the installation of the Advanced Camera for Surveys (ACS), we carried out a much deeper photometric probe in a field 38 kpc SSE of the center, with sufficiently faint limits to detect the core helium burning stars located in the red clump (Rejkuba et al. 2005). This deep view of the halo not only further confirmed the metal-rich nature of the halo stars, but also permitted a quantitative estimate of the halo age distribution: 70−80% of the stars formed 12±1 Gyr ago, and the remaining 20−30% population is best fit with 2−4 Gyr old models (Rejkuba et al. 2011, henceforward R11). Remarkably, these deep data indicate that the full metallicity range of the models ($Z = 0.0001-0.04$) combined with old ages needs to be used to reproduce the colors of the reddest RGB stars in this field.

The last *Hubble* servicing mission 4 enabled imaging with a wider field of view by combining the newly installed Wide Field Camera 3 (WFC3) in parallel with ACS. We designed a program to map five pairs of new locations in the outer halo of NGC 5128, two along the minor and three along the northeastern major axis, with the intention of exploring the extent of the halo and the properties of the stars located in its most extreme regions. The first results from this program were summarized briefly in Rejkuba et al. (2014, Paper I). We found a transition from a metal-rich inner galaxy to a lower-metallicity outer halo, with a shallow metallicity gradient and hints of possible substructures in the outer halo based on metallicity and number density variations in neighboring parallel fields. The shape of the halo was found to be elongated (roughly consistent with the inner halo), with an excess of stars along the major axis above the $r^{1/4}$ law fit to the star counts from earlier HST studies. Most remarkably, halo RGB stars are still present in fields as far out as 140 kpc (25 effective radii $R_{\rm e}$) along the major axis, and 90 kpc (16 $R_{\rm e}$) along the minor axis. In short, no clear 'end' to this galaxy halo has been found.

Complementing the narrow pencil-beam studies conducted with the HST, the extended halo of NGC 5128 was also surveyed from the ground with the VIMOS[1] optical imager on the 8 m ESO VLT (Crnojević et al. 2013; Bird et al. 2015). The Magellan Megacam imager at Las Campanas Observatory was used to observe NGC 5128 (Crnojević et al. 2016a) as part of the Panoramic Imaging Survey of Centaurus and Sculptor (PISCeS; Crnojević et al. 2016b). These wide surveys uncovered a vast amount of substructure, including several dwarfs in the process of being accreted. This process creates overdense regions in the halo. However, the intermediate Galactic latitude of NGC 5128 unfortunately means that large numbers of foreground stars are present, which adds to unresolved background galaxies. When the field contamination issue is combined with uneven completeness due to observations taken under a range of observing conditions, studying its halo properties based on RGB star counts is challenging from the ground. We believe that the best way forward is to combine the strengths of the wide-area surveys that provide a global view of the halo and substructure with the higher resolution and deeper observations from space that enable detailed investigation of its stellar composition.

Since our last HST-based study (Paper I), new ACS and WFC3 imaging was secured that primarily focused on confirming the newly discovered dwarf galaxies and substructures (Crnojević et al. 2019), but also added further parallel pointings in the halo of NGC 5128. Armed with the information from the recent wide-area PISCeS survey of the Cen A halo, we assembled all HST observations taken so far to present a homogeneous analysis of the radial structure of the halo, its metallicity distribution, and metallicity gradients across a vast area of the halo of NGC 5128.

In this paper we describe in more detail the data and photometric measurements done for the Cycle 20 observations, for which initial results were presented in Paper I. We add 15 more

[1] VIsible MultiObject Spectrograph (VIMOS) was mounted on the Unit Telescope 3 (UT3) of the Very Large Telescope (VLT) at the European Southern Observatory (ESO) Paranal Observatory and it included imaging in addition to its primary spectroscopic modes.

Table 1. HST observations of the NGC 5128 halo fields.

Field ID [(1)]	Date yyyy-mm	Prg. ID	Exptime $F814W$ (s)	Exptime $F606W$ (s)	HST camera	RA J2000 hh:mm:ss	Dec J2000 dd:mm:ss	$E(B-V)$ (mag)	R (kpc)	θ_a (deg)	a/R_e
F1	1999-06	8195	12 100	17 500	WFPC2/PC	13:24:51	−43:04:33	0.121	8.3	152.0	1.8
F2	1997-08	5905	12 800	12 800	WFPC2/WF	13:25:29	−43:19:09	0.115	20.0	−144.2	4.8
F3	1999-07	8195	17 500	17 800	WFPC2/WF+PC	13:25:16	−43:28:01	0.123	29.9	−149.5	6.8
F4	2002-07	9373	30 880	30 880	ACS/WFC	13:25:15	−43:34:30	0.123	37.1	−149.0	8.4
F5A	2013-05	12964	2137	2270	ACS/WFC	13:27:32	−42:12:24	0.115	59.8	10.0	11.0
F5W	2013-05	12964	2376	2496	WFC3/UVIS	13:28:01	−42:14:37	0.113	60.5	3.9	10.8
F6A	2013-01	12964	2137	2270	ACS/WFC	13:29:19	−41:56:51	0.141	85.7	1.7	15.2
F6W	2013-01	12964	2376	2496	WFC3/UVIS	13:29:10	−41:51:21	0.139	90.0	4.8	16.0
F7A	2013-06	12964	2137	2270	ACS/WFC	13:31:12	−41:11:57	0.091	140.5	5.0	25.0
F7W	2013-06	12964	2376	2496	WFC3/UVIS	13:31:29	−41:16:45	0.093	137.8	2.7	24.4
F8A	2013-05	12964	2137	2270	ACS/WFC	13:22:52	−42:44:49	0.139	36.5	95.1	11.9
F8W	2013-05	12964	2376	2496	WFC3/UVIS	13:23:20	−42:47:10	0.143	30.3	94.1	9.9
F9A	2013-01	12964	2137	2270	ACS/WFC	13:20:42	−42:35:19	0.158	64.9	98.7	21.1
F9W	2013-01	12964	2376	2496	WFC3/UVIS	13:20:30	−42:30:00	0.144	69.9	95.2	22.8
W1	2015-08	13856	1278	1210	WFC3/UVIS	13:30:21	−41:58:43	0.110	91.8	−5.7	16.4
W2	2016-01	13856	1278	1210	WFC3/UVIS	13:29:51	−41:47:41	0.112	97.9	1.8	17.3
W3	2015-06	13856	1278	1210	WFC3/UVIS	13:23:18	−41:51:02	0.110	82.3	53.7	23.4
W4	2015-06	13856	1278	1210	WFC3/UVIS	13:20:08	−42:03:27	0.107	91.6	80.4	29.6
W5	2015-06	13856	1278	1210	WFC3/UVIS	13:26:12	−41:09:35	0.094	124.3	30.84	28.2
W6	2016-01	13856	1278	1210	WFC3/UVIS	13:26:29	−42:38:31	0.096	28.1	8.6	5.1
W7	2015-06	13856	1278	1210	WFC3/UVIS	13:27:07	−43:03:44	0.089	20.2	−63.1	6.2
W8	2015-04	13856	1278	1210	WFC3/UVIS	13:26:51	−43:30:40	0.099	36.9	−117.7	11.1
W9	2015-04	13856	1278	1210	WFC3/UVIS	13:24:33	−43:25:25	0.114	29.1	−167.4	5.5
W10	2015-04	13856	1278	1210	WFC3/UVIS	13:24:29	−43:23:30	0.116	27.5	−170.6	5.0
W11	2015-06	13856	1278	1210	WFC3/UVIS	13:24:39	−43:19:50	0.115	23.0	−170.4	4.2
W12	2015-04	13856	1278	1210	WFC3/UVIS	13:24:40	−43:19:37	0.115	22.7	−170.2	4.2
W13	2015-06	13856	1278	1210	WFC3/UVIS	13:21:57	−43:08:40	0.130	43.5	136.1	11.4
W14	2016-01	13856	1278	1210	WFC3/UVIS	13:24:06	−42:03:37	0.106	66.1	49.5	18.1
W16	2015-06	13856	1278	1210	WFC3/UVIS	13:30:06	−43:35:15	0.117	67.8	−88.8	22.3
F10A [(2)]	2018-04	15426	2228	2379	ACS/WFC	13:17:47	−44:12:24	0.096	121.8	165.2	23.4

Notes. Columns RA and Dec report the center of the field coordinates, $E(B-V)$ is the reddening value toward the field center based on Schlegel et al. (1998) reddening maps, and R is the projected radial distance in kpc from the center of the galaxy. In the last two columns, θ_a is the azimuthal angle of the field location measured clockwise from the isophotal major axis (see Fig. 1), while a is the semimajor axis of the elliptical isophote that goes through the field (assuming $e = 0.54$ ellipticity) in units of $R_e = 305'' = 5.6$ kpc. [(1)]Our numbering of the Wxx fields in the first column (Field ID) follows the MAST Archive listing, in which there is no "W15". [(2)]The field F10A listed at the bottom is used as a background control field (see Sect. 3.2).

halo fields that were obtained as Parallel pointings within the more recent Cycle 22 and Cycle 25 HST programs (PI: Crnojević), essentially doubling the database. We also carry out a homogeneous analysis of all these halo locations. These parallel fields were only used as control fields for the dwarf galaxy CMD analysis by Crnojević et al. (2019) and were not analyzed in terms of their contribution to the overall stellar halo properties before. Furthermore, we discuss the foreground and background field contamination using several methods: a control field, Milky Way models, and a combination of optical and near-IR photometry. We finally adopt a statistical decontamination of our CMDs based on the control field. From the newly calibrated and decontaminated CMDs, we derive a new self-consistent surface-density profile extending outward to the currently detectable limits of this galaxy's giant halo and measure the stellar halo ellipticity. We discuss the possible presence of intermediate-age asymptotic giant branch (AGB) stars in the halo by analyzing the numbers of stars populating the CMDs just above the RGB tip.

Throughout the paper, we adopt the distance to NGC 5128 of 3.82 Mpc (distance modulus $(m - M)_0 = 27.91$ mag), which is based on average distances from four well-established distance determination methods: the Cepheid period-luminosity relation, TRGB, the planetary nebulae luminosity function, and the Mira variables period-luminosity relation (see Harris et al. 2010 for detailed discussion of the distance determinations). Based on the intrinsic brightness of the RGB tip M_I(TRGB) = −4.05 (Rizzi et al. 2007; Freedman et al. 2020), the TRGB in NGC 5128 fields is found at $I_0 = 23.86$ mag.

2. Data

2.1. HST imaging observations

In Table 1 we list the basic information about all HST fields used in this study[2]. Their distribution on the sky, in a coordinate system centered on NGC 5128, is shown in Fig. 1. In the right panel we also show the unsharp-masked image from Peng et al. (2002). The comparison emphasizes the wide span of the halo probed by our target fields, most of which lie far beyond the inner regions (i.e., the inner square in Fig. 1) containing arcs and shells, dust, and star-forming regions that are remnants of the

[2] Additional images for other fields in NGC 5128 exist in the HST archive, but they are unsuitable for a homogeneous analysis because of one of the following reasons: (i) located at the center of known overdensities (Crnojević et al. 2019), (ii) are not deep enough, or (iii) were obtained with different filters, or only in one filter.

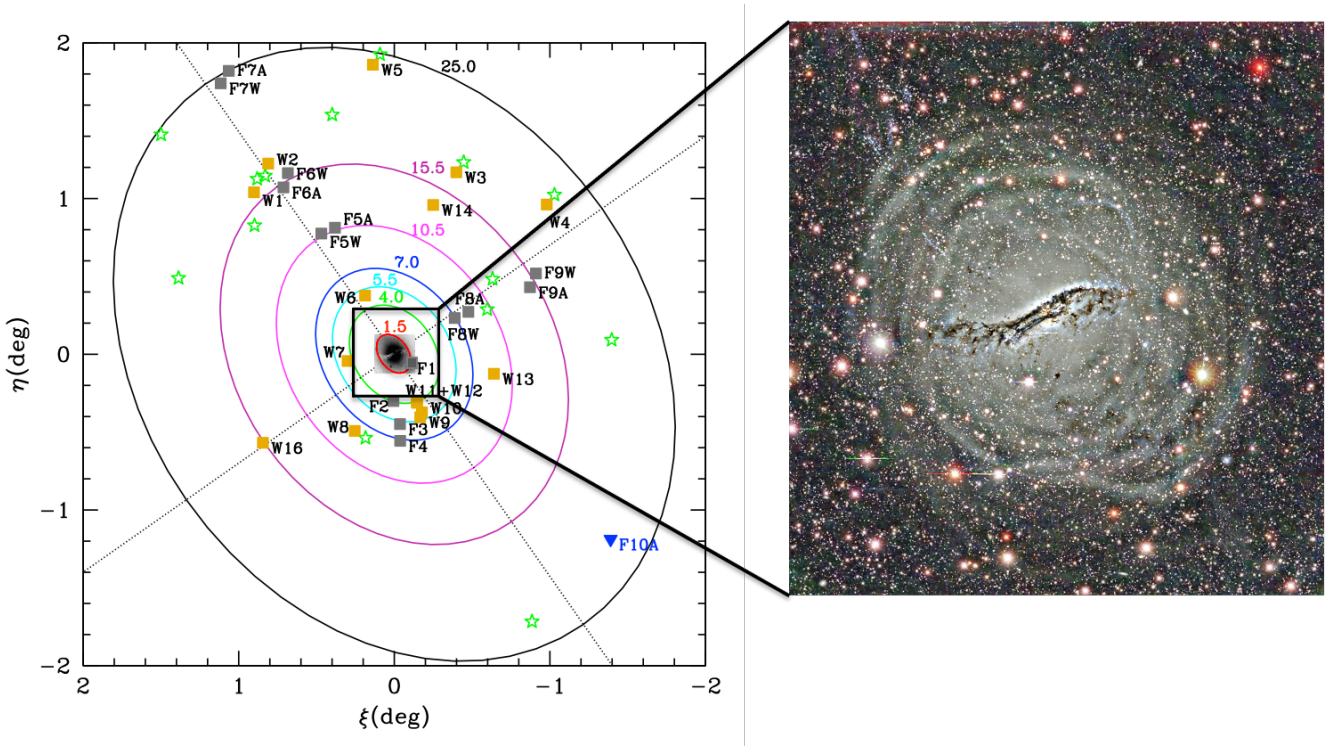

Fig. 1. Distribution of the fields imaged with the HST in $F606W$ and $F814W$ filters as listed in Table 1 relative to the center of NGC 5128 projected on the plane of the sky. Gray squares are fields F1–F9, orange squares are for WFC3 parallels W1–W16 from GO13856, and the blue inverted triangle is for the ACS parallel from GO15426. North is at the top and east at the left. The halo isophotal major axis is oriented 35° east of north (counterclockwise; Dufour et al. 1979). The elliptical contours have an axis ratio of 0.77 as determined from the inner halo (Dufour et al. 1979) and are plotted for 1.5, 4, 5.5, 7, 10.5, 15.5, and 25 R_e distance (as indicated). The green stars are dwarf galaxies in the Cen A group as listed in Table 4 in Müller et al. (2019). Most of them have recently confirmed Cen A group membership based on the primary pointings from GO13856 (Crnojević et al. 2019). The large black square in the center indicates the relative size of the $35' \times 35'$ (38.6×38.6 kpc^2) unsharp-masked image of the shells in the central parts of the galaxy shown in the *right panel* (Peng et al. 2002, image credit: Eric Peng (JHU), Holland Ford (JHU/STScI), Ken Freeman (ANU), Rick White (STScI), and NOAO/AURA/NSF).

recent merger episode(s). Concerns about contamination of our target fields from these factors are thus mitigated. By contrast, we need to be aware of possible contamination from the presence of outer-halo dwarf satellites and substructure (Crnojević et al. 2016a). We show therefore in Fig. 1 the location of known dwarf satellites of Cen A within the area covered by our HST fields. Having effective radii between ∼150 and 600 pc, these dwarfs typically cover up to ∼1′ on sky[3] and thus do not contribute stars to adjacent parallel pointings. One exception is the CenA-MM-Dw3 stream (Crnojević et al. 2019) that crosses one of our fields. This is further discussed below.

The observations of the inner WFPC2 fields F1–F3 taken within HST Cycles 5 and 8 were described in detail by Harris et al. (1999) and Harris & Harris (2000, 2002), while field F4 is our deepest probe into the halo population, where the ACS photometry reached the core-helium burning stars (Rejkuba et al. 2005, 2011). This deep field received 12 orbit-long exposures for each of the two filters. The fields F5–F9 are from our Cycle 20 data (Paper I) and have two entries each, one for the WFC3 camera (e.g., F5W), and the other for the ACS (e.g., F5A) images taken in parallel mode. The Cycle 20 observations were organized such that two orbits for each target were placed within a spacecraft visit to obtain the images in two filters at the same field orientation. Within each orbit, a set of three dithered images using the WFC3-UVIS-DITHER-LINE-3PT pattern were taken for each filter.

Fields W1–W16 are the WFC3 observations from the Cycle 22 program GO13856 (PI: Crnojević). In this program, ACS fields were placed on faint dwarf satellites (Crnojević et al. 2019), while the WFC3 data were the parallels located on blank halo fields adjacent to them. The two cameras are separated by more than 5′ in the focal plane of the HST, corresponding to a linear separation of ∼5.5 kpc center to center at the distance of NGC 5128. This distance is much larger than the physical dimensions of any of the dwarf satellites, therefore the W1–W16 pointings are expected to sample pure field halo populations. Fields W11 and W12 heavily overlap in location due to the closeness of the primary ACS targets, and there is no W15 field (see Table 1). The Wxx set therefore really just covers 14 independent pointings.

Finally, we added one more field (F10A, listed in the last row of Table 1). This is the parallel image from program GO15426 (PI Crnojević) taken with the ACS, located on a remote halo field ∼120 kpc to the southwest. As we describe below, it provides us with what is likely to be the best available control field for gauging the field contamination.

For all the targets listed in Table 1, the filters were $F606W$ and $F814W$, which transform well into (V, I) and which provide a color index $(V - I)$ that is reasonably sensitive to metallicity for old RGB stars over the entire range from [Fe/H] ≃ −2 dex to above-solar abundance. The "Exptime" columns in Table 1

[3] 1′ at the distance of Cen A corresponds to ∼1.1 kpc.

report the total exposure time per filter (for F5–F9, these are essentially full one-orbit exposures, while for W1–W16, they are half-orbit exposures, leading to slightly shallower CMDs). The camera(s) that were used determine the total field of view (FOV) per field: for F1 (WFPC2/PC1), this is as small as 0.3403 arcmin^2, F2 covers 5.33 arcmin^2, and F3, which combines all four WFPC2 detectors, reaches 5.674 arcmin^2. For the rest, the ACS camera FOV is 11.33 arcmin^2, and WFC3 covers 7.29 arcmin^2.

In total the target fields span almost 4° across the sky. We therefore expect differences in Galactic (Milky Way) foreground extinction from one field to the next that are large enough to call for individual correction. The adopted Galactic extinctions toward each field are listed in Table 1 and are computed from the Schlegel et al. (1998) reddening value $E(B-V)$ adopting the Schlafly & Finkbeiner (2011) recalibration[4] and $A_V = 2.79 * E(B-V)$, $A_I = 1.55 * E(B-V)$.

Table 1 also gives the on-sky projected radial distance R in kiloparsecs from the center of NGC 5128[5] assuming an intrinsic distance modulus $(m-M)_0 = 27.91$ (Harris et al. 2010). The position angle θ_a is the azimuthal angle (measured north of east, or clockwise in the figure) from the major axis a (where the ellipticity is $e = (b/a) = 0.54$, see Sect. 4 below). Here a is listed in units of R_e, where we adopt $R_e = 305'' = 5.6$ kpc from Dufour et al. (1979) as determined from the integrated-light profile of the inner spheroid.

2.2. Photometry

All observations used the same filters ($F606W, F814W$) and the photometric data reduction procedures were the same. We started from the pipeline processed *.drc images downloaded from the HST archive that are the multidrizzled combinations of the individual exposures including CTE corrections. While the stars in the target halo fields are quite uncrowded in any absolute sense and aperture photometry would be possible for them, we preferred to run the *daophot* and *allstar* suite of photometric codes in IRAF (Stetson 1987) to perform the photometry via PSF fitting. In addition to a homogeneous procedure applied to all fields, this gives us the advantage of having stellar PSF-fitting parameters that can be used to distinguish objectively between slightly resolved background galaxies and point sources.

In each field, a master image consisting of all exposures in both filters was constructed to provide the deepest possible source for object detection. SourceExtractor (Bertin & Arnouts 1996) was used on the master image to detect candidate objects and perform a preliminary culling out of nonstellar objects (half-light radii $r_{1/2} < 1.0$ or >1.6 px were rejected). From there, *daophot* was used to carry out small-aperture ($r = 2$ px) photometry, construction of a PSF for each filter, and then final photometry with *allstar*. The independently determined PSFs on each field were built from typically 30 to 70 individual bright uncrowded stars. Although these proved to be quite consistent with each other, in the end, to improve internal consistency, exactly the same set of ($F606W, F814W$) PSFs picked from the highest S/N cases for a given camera and filter were used on all the fields. Further culling of the starlists was done by rejecting any objects with *allstar* parameters $\chi > 2$ or $err > 0.2$ mag in either filter. Because crowding is not a factor, any such rejected objects are almost always nonstellar. Empirically derived aperture corrections to $r = 10$ px were added to the *allstar* measured magnitudes, and the large-aperture data were then converted into filter magnitudes ($F606W, F814W$) with filter zeropoints from the ACS or WFC3 webpages. These were finally converted into standard (V, I) with the linear color transformations noted below.

2.3. Calibrations for the ACS and WFC3 photometry

Our photometric calibration for the ACS fields follows the prescription in Sirianni et al. (2005) and is on the VEGAMAG system. To bring the instrumental magnitude measurements to the HST system, we used the zeropoint calculator published on the HST web pages. We applied the following calibration equations:

$$F606W = -2.5 \times \log \frac{f606w_{\rm inst}}{\rm exptime} + zpt_{F606W} + apcor_{F606W} \quad (1)$$

$$F814W = -2.5 \times \log \frac{f814w_{\rm inst}}{\rm exptime} + zpt_{F814W} + apcor_{F814W}, \quad (2)$$

where $zpt_{\rm filter}$ is the VEGAMAG zeropoint for the given filter, and $apcor_{\rm filter}$ is the corresponding aperture correction from our PSF measurement to a 10 px aperture, and then from 10 px to infinite radius (Bohlin 2012). For the ACS data, $zpt_{F606W} = 26.407$ and $zpt_{F814W} = 25.523$.

For the WFC3 camera, the aperture correction to 10 px = 0.″4 radius was made, after which filter zeropoints can be applied that already include the step to infinite radius. We adopted $zpt_{F606W} = 25.8843$, $zpt_{F814W} = 24.5730$.

In Paper I we used the WFC3 zeropoints from the HST webpages to convert the ($F606W, F814W$) magnitudes into (V, I), but out of temporary necessity, we applied the color terms (c_1) for the same filters from the ACS/WFC detector. Since then, Sahu et al. (2014) provided additional data for WFC3/UVIS, listing the zeropoint differences $(I - F814W), (V - F606W)$ for stars over a range of blackbody temperatures and spectral types. By plotting these differences versus $(V-I)$, we reconstructed the color terms in the Vegamag system for the transformations. As with ACS, the slope of the color term c_1 is very small for I, but for V, it appears to be slightly shallower than for the ACS. The transformations for WFC3 that we adopt here are

$$(V - I) = 1.1396 \times (F606W - F814W) \quad (3)$$

$$V = F606W + 0.1545 \times (V - I) \quad (4)$$

$$I = F814W + 0.032 \times (V - I). \quad (5)$$

Empirical transformations of the standard WFC3 filters into BVI have also been derived by Harris (2018) from combined ACS and WFC3 photometry in a 47 Tucanae standard field; encouragingly, for $F606W$ and $F814W$, these are quite similar to those given above. The effect of adopting the revised transformations above was to make the $(V - I)$ colors from WFC3 bluer than in Paper I by typically $\Delta(V - I) \simeq 0.1$ mag. This shift brings the CMDs for ACS and WFC3 into closer agreement.

2.4. Completeness and photometric error analysis

The *addstar* task in *daophot* was used to measure the detection completeness of our photometry and the internal measurement uncertainties. Artificial stars (scaled PSFs) were added, 1000 at a time, into the images, and we then remeasured with exactly the same procedures as described above. The completeness f is the recovery fraction: the number of artificial stars detected in a given magnitude bin divided by the number of artificial stars inserted. A sample of the fraction of recovered

[4] Source: http://irsa.ipac.caltech.edu/applications/DUST/

[5] $RA_0 = 13{:}25{:}27.6$, $Dec_0 = -43{:}01{:}09$ from NED.

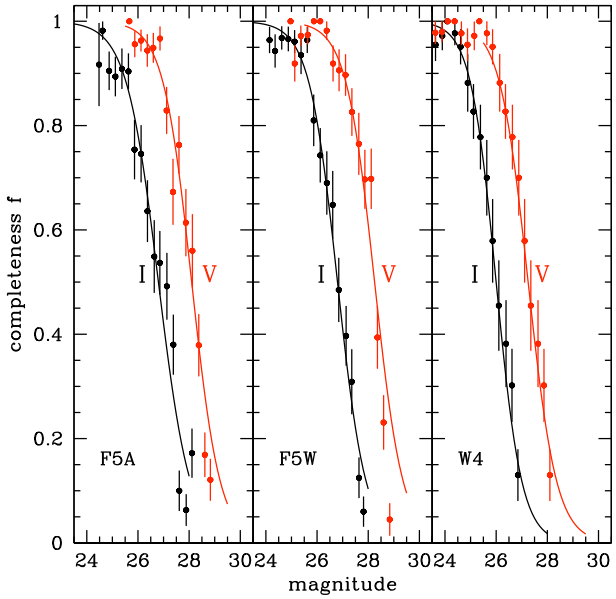

Fig. 2. Samples of *daophot/addstar* experiments for three different fields in our study. The completeness fraction f is plotted vs. V or I magnitude in each panel. The measured f-values per 0.25-mag bin are shown as the black (I) or red (V) points with error bars. The solid lines (black for I, red for V) show the smooth fitted curves of the form $f = 1/(1+e^{\alpha(m-m_0)})$ described in the text.

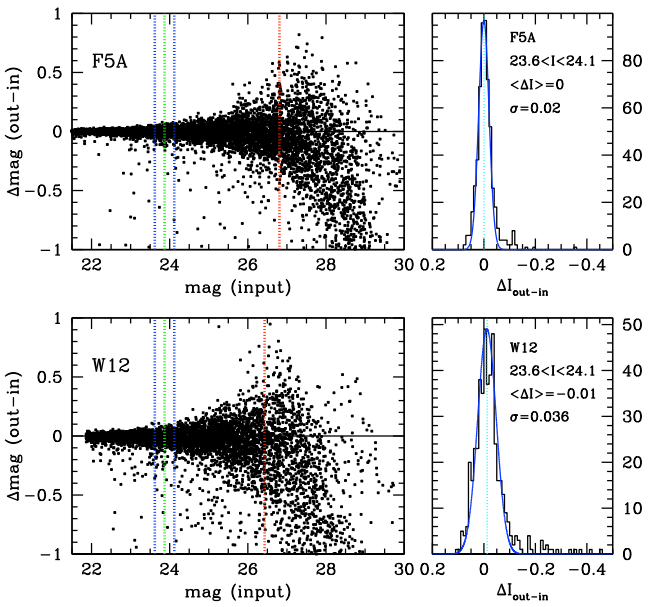

Fig. 3. Sample of photometric measurement precision for Field F5A (*top*) and W12 (*bottom panels*) for the I band. The magnitude difference $\Delta(m)$ (measured – input) for 10 000 input artificial stars is plotted against input magnitude for F5A (*upper left*) and W12 (*lower left panel*). The 50% detection completeness levels are marked with the vertical dotted red lines. The dotted green line is the magnitude of the TRGB. The blue lines indicate ±0.25 mag around the TRGB. *Right panels*: distributions of magnitude differences (measured – input) for stars within ±0.25 mag of the TRGB, binned to 0.01 mag for F5A (*upper right*) and W12 (*lower right panel*). The Gaussian curves plotted over the magnitude difference histograms have the mean and sigma as indicated in the panels.

Table 2. Photometric uncertainty and completeness parameters.

Parameter	12964(ACS)	12964(WFC3)	13856(WFC3)
α_V	1.8	1.8	1.8
$m_{0,V}$	28.1	28.25	27.70
α_I	1.6	1.8	2.0
$m_{0,I}$	26.8	26.8	26.42
$\beta_{0,V}$	0.02	0.02	0.035
$\beta_{1,V}$	0.053	0.056	0.063
$\beta_{2,V}$	27.0	27.0	27.0
$\beta_{0,I}$	0.02	0.02	0.025
$\beta_{1,I}$	0.050	0.042	0.050
$\beta_{2,I}$	25.5	25.5	25.0

stars versus magnitude is shown in Fig. 2, for the three different combinations of filter and exposure time that we have (the ACS fields from GO12964, WFC3 from GO12964, and WFC3 from GO13856). Completeness experiments for fields F1–F4 are described in detail in the papers that reported their initial analysis (Harris et al. 1999; Harris & Harris 2000, 2002; Rejkuba et al. 2005).

As is typical for very uncrowded images such as we have here, the detection fraction declines smoothly from near-100% down to near-zero over a two-magnitude run. Analytic curves of the form $f = 1/(1 + e^{\alpha(m-m_0)})$ (Harris et al. 2016) are superimposed on the data in Fig. 2. In this relation, m_0 represents the magnitude where $f = 0.5$, and α represents the steepness of decline. Table 2 lists the pairs of parameters for the three sets of images. The most important feature of the adopted completeness curves is that they accurately describe the shape of $f(m)$ for $f > 0.5$; we did not use any data below this 50% point.

The exposure times and therefore also the completeness are comparable for F10A (GO15426) and for the Cycle 20 data from GO12964. As expected, with respect to these, m_0 is about one magnitude brighter than for the fields in GO13856, which have half the exposure time of the other two sets. As we show below, however, this difference does not seriously hamper our goals to derive the halo RGB population density.

The artificial star tests were also used to determine the measurement uncertainties of the data. Sample artificial star runs showing the recovered magnitudes compared with their input values are shown in Fig. 3 for a range of magnitudes between ~2 mag brighter than the TRGB down to well below the completeness limit. These tests showed that to a close approximation, the measurement uncertainties are about 1.4 times larger than the numbers returned by daophot/allstar. A useful interpolation equation for the dependence of measurement uncertainty on magnitude is

$$e_m = \beta_0 + \beta_1 e^{(m-\beta_2)}, \quad (6)$$

where the β-values appropriate for the different sets of exposures are listed in Table 2.

The artificial star tests can also be used to check for the possible presence of blends. These are stars that are measured brighter due to underlying (unresolved) background and thus shift to brighter bins in the luminosity function. In the right panels of Fig. 3 we show the difference of magnitude (measured–input) for stars within ±0.25 mag of the TRGB. The tail of the distribution extending to negative (brighter measured) magnitudes is negligibly small even in our most densely populated field (W12), and

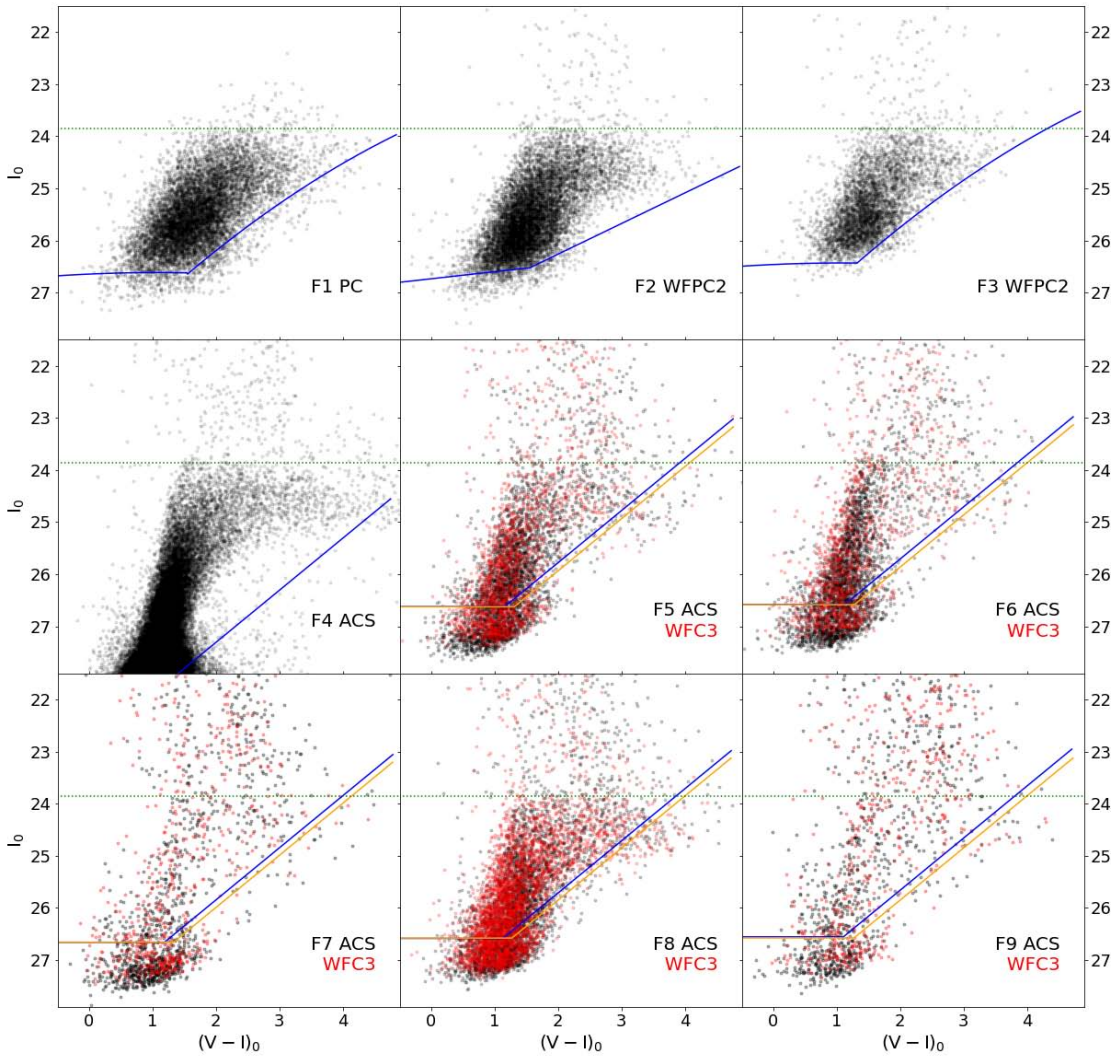

Fig. 4. Measured CMDs for fields F1–F9 as listed in Table 1, including the correction for Galactic extinction. The older data for locations at 8, 20, and 30 kpc (F1, F2, and F3) were taken with the WFPC2 camera. For the fields F5 to F9, data from ACS pointings are plotted as black dots and from WFC3 as red dots. The solid lines show the 50% detection completeness levels (ACS and WFPC2 in blue, and WFC3 in orange). The dotted green line indicates the expected location of the TRGB. For F4, the photometric limits are much deeper than for the other fields.

it is completely absent in a typical halo field (F5A). The mean magnitude of measured stars is 0.01 mag brighter for W12 field, and it shows no systematic shift for less populated fields.

3. Color-magnitude diagrams

The CMDs for our complete set of fields are shown in Figs. 4 and 5. In Fig. 4, a small but important check on the internal consistency of our photometry is that for each pair of ACS/WFC3 fields, the CMDs overlie each other closely, within the scatter of points along the RGB in each field. Here, they match better than we found in Paper I, a direct result of the improved WFC3 color transformations in the present work.

A broad RGB component is present in all fields, as is the clear TRGB located at $I_0 \simeq 23.86$ (indicated with the dotted green line) and slanting downward at redder colors due to increasing bolometric correction. A population of foreground stars is also clearly present in all fields over a wide range of colors, and it extends well above the RGB population. In the outermost fields (e.g., W3, W4, W5, and W16), the contamination appears to be comparable to the number of NGC 5128 stars. Therefore the first necessary task for the analysis is to remove this contamination as well as possible so that unbiased measures of the radial density distribution can be made.

The field contamination is due to a combination of foreground stars and very small, faint background galaxies that managed to pass the selection criteria described above. Although the well-populated inner fields are completely dominated by the NGC 5128 halo RGB stars and thus contamination is of relatively little concern, for our outermost fields, the objective removal of contaminants is critical.

It is possible to model the foreground population of Milky Way stars as a function of the position on the sky, but faint background galaxies provide more of a challenge. In the following, we first discuss the bright foreground stellar component in comparison with the Milky Way stellar population models. This is used to evaluate the ability of the models to reproduce the foreground Milky Way component and also to assess the possible presence of a bright AGB component in the halo of NGC 5128. A contribution from bright AGB giants is expected in some inner

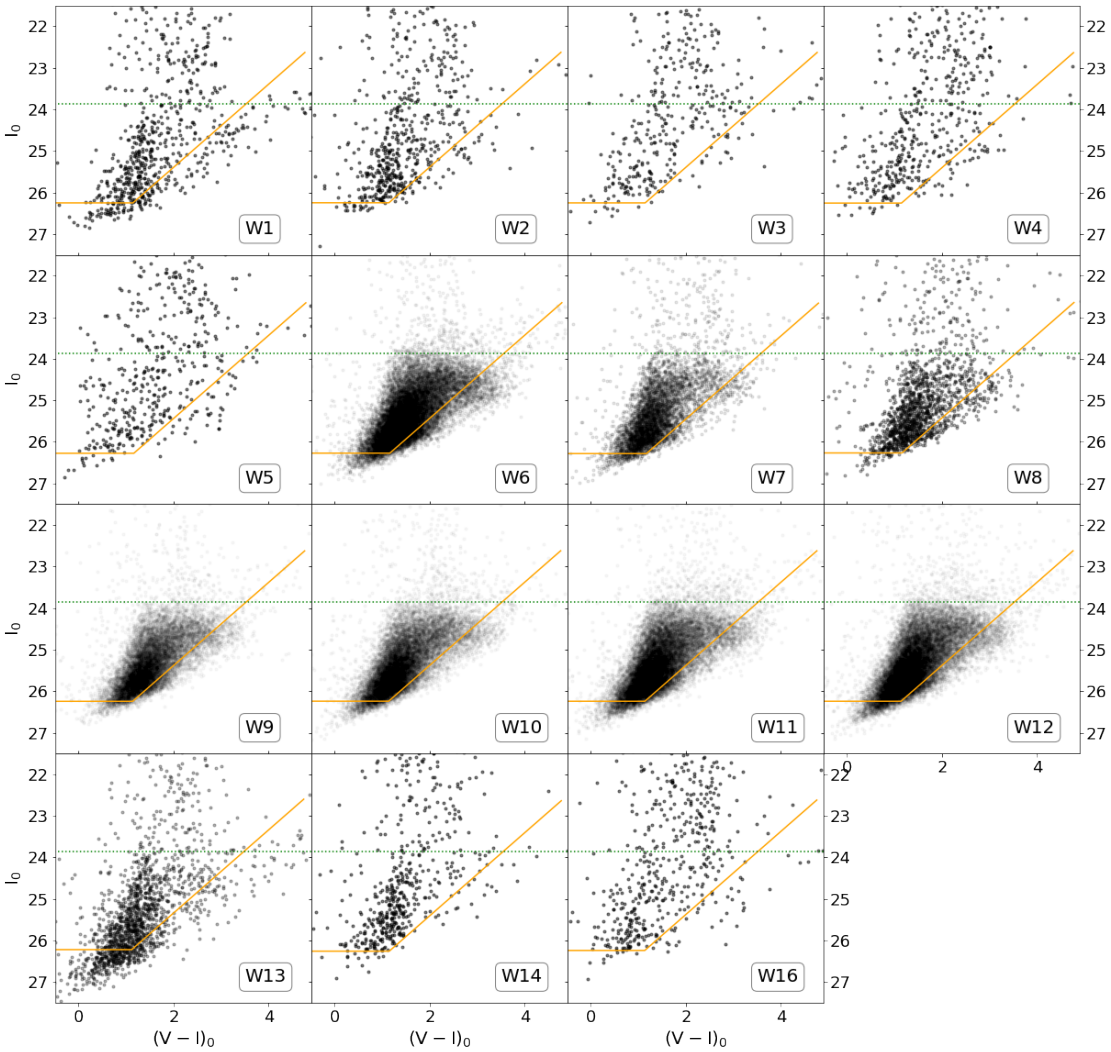

Fig. 5. CMDs for fields W1–W16 corrected for Galactic extinction. These fields have half the exposure time of F5–F9 and thus have brighter limiting magnitudes and noticeably brighter completeness cutoff levels in the bluer filter. The solid (orange) lines show the 50% detection completeness levels. The dotted green line indicates the expected location of TRGB.

fields given the detection of a population of bright long period variable (LPV) stars (Rejkuba et al. 2003a) and intermediate-age globular clusters (GCs) (Woodley et al. 2010), but it is so far unknown how far it extends into the halo (see also the discussion in Crnojević et al. 2013). The population of contaminants in the CMD can also be evaluated empirically. In Sect. 3.2 we describe this alternative method, which we eventually preferred and adopted for the remaining analysis.

3.1. Modeling the foreground component

Models of the Milky Way stellar population can be used to simulate the number of stars and their magnitude-color distribution along the line of sight of NGC 5128. In Paper I we adopted the TRILEGAL (Girardi et al. 2005) simulation because it had a higher density of faint stars than the Besançon (Robin et al. 2003) model. In this paper we explore in more detail the ability of the TRILEGAL model to reproduce the foreground Milky Way population in comparison with our data (see also Appendix A). In order to avoid issues with different completeness due to different exposure times, we restrict the comparison of the models to the fields observed during Cycle 20 (F5–F9).

The TRILEGAL simulator prompts for many different inputs. Keeping the parameters of the galactic components to their default values, we simulated a field of 0.026 square degrees, equal to the total surveyed area of 5 ACS + 5 WFC3 pointings observed during Cycle 20, in the direction of the NGC 5128 coordinates. Most of the simulated objects are main-sequence stars, but with a few white dwarfs populating the bluer colors of the distribution.

The TRILEGAL model with a Chabrier IMF and a binary fraction of 0.3 (Fig. 6) has 1128 stars in the magnitude range $19 < I < 22$. In the same magnitude range, the Besançon model has 1097 stars. The models obtained with other prescriptions have a slightly different number of stars in this range, although these differences may reflect the normalization of the TRILEGAL simulator. To compare the simulations among themselves, we normalized their counts in the range $20 < I < 22$. The simulations adopting different options (e.g., binaries on or off) yield similar results, except for the case of a Salpeter IMF, in which a large component of faint ($I \gtrsim 25$) and red ($V - I \gtrsim 3$) dwarfs